Measurement report: New insights into the mixing structures of black carbon on the eastern Tibetan Plateau: soot redistribution and fractal dimension enhancement by liquid–liquid phase separation

Qi Yuan[1, 8], Yuanyuan Wang[2], Yixin Chen[2], Siyao Yue[3, a], Jian Zhang[4], Yinxiao Zhang[5], Liang Xu[6], Wei Hu[7], Dantong Liu[2], Pingqing Fu[7], Huiwang Gao[1], Weijun Li[2*]

[1]Key Laboratory of Marine Environmental Science and Ecology, Ministry of Education of China, Ocean University of China, Qingdao 266100, Shandong, China
[2]Department of Atmospheric Sciences, School of Earth Sciences, Zhejiang University, Hangzhou 310027, Zhejiang, China
[3]State Key Laboratory of Atmospheric Boundary Layer Physics and Atmospheric Chemistry, Institute of Atmospheric Physics, Chinese Academy of Sciences, Beijing 100029, China
[4]School of Environmental and Material Engineering, Yantai University, Yantai 264005, Shandong, China
[5]Flight College, Binzhou University, Binzhou 256600, Shandong, China
[6]College of Sciences, China Jiliang University, Hangzhou 310018, Zhejiang, China
[7]Institute of Surface-Earth System Science, School of Earth System Science, Tianjin University, Tianjin 300072, China
[8]Key Laboratory of Atmospheric Chemistry, China Meteorological Administration, Beijing 100081, China
[a]Now at: Max Planck Inst Chem, Minerva Res Grp, D-55128 Mainz, Germany

Correspondence: Weijun Li (liweijun@zju.edu.cn)

Abstract. Black carbon (BC, i.e., soot) absorbs radiation and contributes to glacier retreat over the Tibetan Plateau (TP). A lack of comprehensive understanding of the actual mixing state leads to large controversies in the climatic simulation of soot over the TP. In this study, ground-based sampling, electron microscopy analyses, and theoretical calculations were used to investigate the interactions among the liquid–liquid phase separation (LLPS), soot redistribution in secondary particles, and fractal dimension (D_f) of soot particles on the eastern rim of the TP. We found that more than half of the total analysed particles were soot-containing particles. One-third of soot-containing particles showed a core-shell structure that probably formed the LLPS phenomenon after long-range transport. Particle size and ratio of organic coating thickness to soot size are two of the major possible factors that likely induce soot redistribution between organic matter and inorganic aerosols in individual particles. The D_f sequence is ranked as externally mixed soot (1.79±0.09) < sulfate-coated soot (1.84±0.07) < organic-coated soot (1.95±0.06). We concluded that the soot redistribution process promoted the morphological compaction of soot particles. This study indicates that soot-containing particles experienced consistent ageing processes that induced a more compact morphology and soot redistribution in the LLPS particles on the remote eastern rim of the TP. Understanding the microscopic changes in aged soot particles could further improve the current climate models and evaluations of BC's radiative impacts on the eastern TP and similar remote air.

1 Introduction

The Tibetan Plateau (TP), known as the "Third Pole", is the highest and largest plateau on Earth (Yao et al., 2012a). Due to the largest reserves of glacial area (~10^5 km^2) beside the polar regions, the TP acts as the "Asian water tower" and plays a crucial role in supplying water for Asian ecosystems and human survival (Immerzeel et al., 2010). The eastern TP, as a source region of several large Asian rivers, has numerous glaciers but exhibits a serious glacial retreat (Yao et al., 2012b). Black carbon (BC, i.e., soot), the most important light-absorbing aerosol from biomass or fuel burning (Bond et al., 2013), is one of the major contributors to the retreat of eastern Tibetan glaciers through deposition on their surfaces (Xu et al., 2009;Li et al., 2016a;Hu et al., 2018;Shao et al., 2017;Dong et al., 2016;Li et al., 2018). Long-term field measurements indicate that BC concentrations exhibit a high level in the eastern TP atmosphere and snow cover (Kang et al., 2022). A 20-yr simulation using GEOS-Chem model has revealed that approximately 35% of surface BC on the TP originates from East Asia, and a strong East Asian summer monsoon leads to large amounts of BC transported from central China (Han et al., 2020). BC from the Sichuan Basin can be transported to the eastern TP by an intensified southwesterly wind or can penetrate to the eastern TP in the planetary boundary layer (Yuan et al., 2020b). Therefore, the long-range transported BC from East Asia to the eastern TP has become a focal point in aerosol research (Kang et al., 2022).

In recent decades, many studies have focused on the climatic effects of BC over the TP (Chen et al., 2022b;Zhu et al., 2021). It is worth noting that the estimation of direct radiative forcing of BC exhibited a large difference in several model studies over the entire TP, such as a four-stream radiative transfer model simulation of +0.29–+2.61 W m^{-2} (Kopacz et al., 2011), a global chemical transport model in conjunction with a radiative transfer model simulation of +2.3 W m^{-2} with an uncertainty of ~70–85% (He et al., 2014), a Community Atmosphere Model Version 5 simulation of +0.31±0.12 W m^{-2} (Zhang et al., 2015), and an Santa Barbara DISORT Atmospheric Radiative Transfer model simulation of +4.6±2.4 W m^{-2} (Liu et al., 2021). This differences and uncertainties in BC radiative forcing are largely caused by the variability of the actual BC-mixing state in most models and in the ambient air (Hu et al., 2021;Zhai et al., 2022;Fierce et al., 2020;Riemer et al., 2019;Adachi and Buseck, 2013), especially across the vast TP's different areas. For instance, Wang et al. (2017a) used measurement data to estimate that coatings (sum of organics, sulfate, nitrate, chloride, and ammonium) led to 40% light absorption enhancement of BC on the central TP. In contrast, Wang et al. (2018) applied the Mie model to simulate an average BC absorption enhancement of up to 1.9 on the southeastern TP. These significant variations in BC absorption enhancement can be attributed to the apparent discrepancy and uncertainty between the model simulations and observations regarding the mixing structures of BC particles (Yuan et al., 2019;Tan et al., 2021;Wang et al., 2021a;Zhao et al., 2017;Fu et al., 2022). Therefore, it is crucial to perform extensive in situ measurements and gain more observational data on mixing states of BC particles to improve the current understanding and simulation of the climatic effect of BC on the eastern TP.

Recently, Zhang et al. (2022) observed, for the first time, a unique mixing structure with multiple BC particles redistributed in organic coatings instead of sulfate cores at a high mountain site in central China. BC redistribution was induced by liquid–liquid phase separation (LLPS), leading to a reduction in the absorption enhancement effect by 28–34% (Zhang et al.,

2022). This interesting finding draws our attention to the mixing structure of BC in similar mountainous areas on the eastern rim of the TP. This raises some new questions: is BC redistribution the case or norm in the ambient air? do BC particles undergo similar redistribution during long-range transport from central China to the eastern TP? If so, BC redistribution should be incorporated into the current climate models to correct the absorption enhancement of BC on the eastern TP. To date, there is no evidence for revealing the redistribution mechanisms of soot particles during aerosol phase separation in eastern TP air. Furthermore, while Yuan et al., (2019) demonstrated that sulfate coating under liquid phase can affect the morphology and compactness of the inner BC, it is unclear whether organic coating after BC redistribution can affect the morphology of the inner BC. These questions must be addressed to enable a more precise simulation of the optical absorption of BC in atmospheric models over the eastern or the entire TP.

In this study, individual particle collection, transmission electron microscopy (TEM), scanning electron microscopy (SEM), and atomic force microscopy (AFM) were comprehensively employed to investigate the mixing structures of soot particles at a mountain site on the eastern fringe of the TP. Theoretical calculations were applied to obtain an important morphological parameter (fractal dimension, D_f) of soot particles in different mixing states. The principal concerns of this study are as follows: (1) Can the redistribution of soot particles occur in the eastern TP atmosphere? (2) What are the key factors that affect the redistribution process of soot particles? (3) How do the morphologies of soot particles transform post-redistribution? The answers to these questions will be helpful to better understand the ageing processes of soot particles under LLPS. The findings can also promote the future evaluation of climatic and environmental effects of anthropogenic aerosols on the eastern TP.

2 Methodology

2.1 Sampling site and meteorological analysis

The sampling site was on the top of Mt. Emei (103.33°E, 29.52°N, 3048 m a.s.l. – above sea level), which is located on the eastern rim of the TP (Fig. 1a). Mt. Emei lies in a transitional zone from the low-altitude, urbanized, and industrial Sichuan Basin on the northern and eastern side to the high-altitude, rural, and remote TP on the western side (Fig. 1). Due to the unique mountain–basin topography and intense anthropogenic activities, the Sichuan Basin is one of the most heavily polluted regions in China (Zhang et al., 2012;Shu et al., 2022;Chen et al., 2022a). We obtained $PM_{2.5}$ and BC column mass density in June-July 2016 from the Giovanni online data system (https://giovanni.gsfc.nasa.gov/giovanni/) (Fig. 1b-c). A high-emission zone in the Sichuan Basin was detected during the sampling period (Fig. 1b-c). Several field and model studies showed that large amounts of anthropogenic air pollutants from the Sichuan Basin could be transported to the eastern TP (Jia et al., 2019;Zhang et al., 2015). Mt. Emei has proven to be a suitable site for investigating the long-range transport of anthropogenic aerosols (Zhao et al., 2020).

Twenty-four-hour backwards trajectories were calculated every 1 h at an ending height of 100 m above ground level by using a Hybrid Single Particle Lagrange Integrated Trajectory (HYSPLIT) (Fig. 1a). According to the HYSPLIT calculation,

there were two dominant backwards trajectory types during the individual particle-sampling period: eastern trajectories from the Sichuan Basin (red trajectories in Fig. 1a) and western trajectories from the TP (blue trajectories in Fig. 1a). Various active fire spots were detected over South and Southeast Asia by the Fire Information for Resource Management System (FIRMS) provided by the MODIS satellite (https://firms.modaps.eosdis.nasa.gov) (Fig. 1a). Meteorological data such as relative humidity (RH), temperature (T), wind speed (WS), and wind direction (WD) were measured and recorded every 5 min by an automated instrument (Kestrel 5500, USA) (Fig. S1).

2.2 Individual particle collection

A DKL-2 sampler (Genstar Electronic Technology, China) was used to collect individual aerosol particles on copper TEM grids covered by carbon film (carbon type-B, 300-mesh copper; Tianld Co., China) and silicon wafers (thickness: 500±10 μm, size: 3×3 mm; LIJINGKEJI, China). We also collected individual aerosol particles onto 47 mm diameter polycarbonate filter membranes (600 nm pore size, Whatman Inc., USA) via a Mini-Vol Sampler (Airmetric, USA) for SEM analysis. The individual particle samples were collected according to the detailed procedures in Yuan et al. (2019). A total of 15 aerosol samples were collected in the summer of 2016 (22 June–09 July). The daily sampling times (Beijing) were 09:00, 15:00, and 22:00, with a sampling duration of 45 min at each time. The copper grids, silicon membranes, and polycarbonate filter membranes were stored in the dry, clean, and airtight containers at 20-25% RH until analysis.

2.3 Electron microscopic analysis

The TEM (JEOL JEM-2100, Japan) was operated at 200 kV to analyse 15 aerosol samples by analysing 4499 aerosol particles to obtain their mixing state and morphology. An energy-dispersive X-ray spectrometer (EDS, INCA X-MaxN 80T, Oxford Instruments, UK) was used to detect elements with compositions heavier than C ($Z \geq 6$). TEM observations directly identified soot structure in most individual particles. However, for some typical soot with thick sulfate coating, we normally put the particles under the electron beam for a longer time to destroy the sulfate coating. Then we further clearly identified the structure of soot core left in the TEM image. RADIUS software (EMSIS GmbH, Germany) was used to measure the morphological parameters of individual particles. To analyse elemental distribution in individual aerosol particles, EDS mapping and line scanning experiments were conducted using scanning TEM (STEM) mode in the JEM-2100F TEM. Further details of TEM analysis can be found in Yuan et al. (2021).

The SEM (Zeiss Ultra 55, Germany) was used to obtain detailed information on the surfaces of individual aerosol particles. To obtain three-dimensional morphological information of individual particles on the substrate, we tilted the sample stage to 75° with accelerating voltage of 10 kV and work distance of 6.6 mm, and then captured the particle images at a magnification of 7000×.

The three-dimensional morphology of the aerosol particles was studied by using an AFM (Dimension Icon, Veeco Instruments, Inc., USA) operated in tapping mode under ambient conditions. The bearing area and bearing volume of each analysed particle can be obtained from the AFM images by Nanoscope analysis software (Chi et al., 2015). The equivalent

circle diameter (ECD, d) and the equivalent volume diameter (EVD, D) were calculated according to the bearing area and bearing volume. As shown in Fig. S2, there is a linear relationship between the ECD and EVD of particles with D=0.4144×d. The sizes and coating thicknesses of secondary particles are calculated based on the EVD and the sizes of soot particles are calculated based on the ECD. The detailed calculation method can be found in supplement (Figs. S2 and S3).

2.4 Fractal dimension of soot particles in different mixing states

The morphology and compactness of soot particles can be characterized by D_f, which is calculated by the scaling law below (Koylu et al., 1995). Several previous studies have applied this method to investigate the morphological variations of soot particles in different regions (Wang et al., 2021c;Yuan et al., 2019):

$$N = k_g\left(\frac{2R_g}{d_p}\right)^{D_f} \quad (1)$$

where N is the total number of soot monomers; R_g is the radius of gyration of individual soot particles; d_p is the average diameter of soot monomers; k_g is the fractal prefactor; and D_f is the mass fractal dimension of individual soot particles. In this study, we employed the ensemble method to obtain a mean D_f of soot particles with different mixing states (Wang et al., 2017b). The uncertainty of the D_f was attributed to the uncertainties in the numbers and diameters of soot monomers, which were mainly manually determined (Pang et al., 2022). The quantification of this uncertainty was expressed by the standard error of the slope given by the mean-square fit (China et al., 2013;Yuan et al., 2019).

In addition to D_f, we also used convexity (*CV*), roundness (*RN*), and aspect ratio (*AR*) to quantify the morphology of soot. The *CV* is a measure of the topological properties of the particle's projection and is the ratio of the projected area of the particle to the area of the convex hull polygon. *RN* is a measure of the ratio of the projected area of the particle to the area of a circle of a diameter equal to the longest dimension. *AR* is the maximum ratio between the length and width of a bounding box. These morphological parameters can be calculated using the methods in China et al. (2013) and Yuan et al. (2019). The uncertainties of *CV*, *RN*, and *AR* were expressed by standard errors of these values in all individual soot particles.

3 Results and discussion

3.1 Mixing states of soot particles on Mt. Emei

We analysed thousands of particles ranging in diameter from 30 nm to 4 μm, and found that approximately 54.2% of the total particles were either externally or internally mixed soot particles, which we define as soot-containing particles (Figs. 2 and S2). This proportion of soot-containing particles was lower than our previous field observations at a rural site on the southeastern TP (64%) (Yuan et al., 2019), but higher than that at a remote site in the central Himalaya (51%) (Yuan et al., 2020a). Our analysis also revealed that the proportion of soot-containing particles was much higher (65.4%) when eastern basin trajectories were prevailing, as opposed to the dominance of western TP trajectories (50.2%) (Fig. S4). The results

indicate that regional anthropogenic emissions, particularly from incomplete fossil-fuel burning in the Sichuan Basin, frequently influenced the upper air layer during the sampling period. This finding is consistent with a similar result obtained from a bulk measurement by Zhao et al. (2020).

Based on the morphologies and mixing states of individual soot-containing particles, we identified three primary types. The first type is externally mixed soot, which we have named simply "soot". Soot has a distinct chain-like aggregate morphology (Fig. 2a) and contain primarily of carbon, with minor amounts of oxygen (Fig. 2b). The second type is internally mixed soot with sulfate, which we have named "S-soot". When viewed under an electron beam, sulfate commonly displays surface bubbles (Fig. S5) and partially or completely coat soot particles (Fig. 2c). More than half of soot-containing particles we analysed were identified as S-soot particles (Figs. 2c and 3a). Finally, the third type of soot-containing particle is core-shell particles with soot in either the core or the coating (Fig. 2e, 2g). The EDS spectrum shows that the coating is most likely to be organic matter (OM) with significantly higher C and lower S content compared to the core (Fig. 2f, 2h). Elemental mapping and line scanning analysis of the core-sell particles all reveal that the coating predominantly contains abundant C, while the inorganic core contains abundant S, N, O, and minor K (Fig. 3). This similar core-shell particles have been identified as "OM-coating structure" (Li et al., 2016b), which were reported in previous field observations and laboratory studies (Adachi et al., 2022;Li et al., 2021;Freedman, 2020;Li et al., 2020;Shi et al., 2008). Consequently, we called soot internally mixed within sulfate core or OM-coating as "S-soot-OM-coating" (Fig. 2e, 2g).

Optical and fluorescence microscopy analyses revealed that the LLPS could occur in individual ambient aerosols, with the presence of two separate phases: inner ammonium sulfate and outer secondary organic material (You et al., 2012). Cryo-TEM measurements further confirmed that the LLPS formed the distinct core-shell structures with sulfate core and OM-coating in ambient aerosols (Altaf et al., 2016;Li et al., 2021). Furthermore, the LLPS particles have been widely observed in Arctic air (Kirpes et al., 2022;Yu et al., 2019), rural and mountain areas (Zhang et al., 2022), and forest air (Li et al., 2020). Therefore, S-soot-OM-coating particles as shown in Figure 2 were likely considered as soot particles mixed with the LLPS particles after long-range transport.

A laboratory study and field observations have shown that LLPS can drive soot in core–shell particles from inside inorganic aerosols to outer organic aerosols, which is called the soot redistribution phenomenon (Brunamonti et al., 2015;Xu et al., 2020;Zhang et al., 2022). It is well known that soot particles typically contains hydrocarbons, polycyclic aromatic hydrocarbons, and partially oxidized organics generated during combustion (Long et al., 2013;Wang, 2011). Moreover, TEM observations revealed a thin amorphous organic coating on carbon nanospheres of fresh soot particles (Buseck et al., 2014). The combustion processes always produce extremely thin organic layers on each soot monomer (Leskinen et al., 2023;Chen et al., 2016). Freedman (2017) showed that the LLPS process can influence surface and interfacial tensions among different phases in individual particles. Therefore, some studies used the intermolecular forces and interactions between similar chemical bonds to explain the phenomenon of soot redistribution in individual particles (Brunamonti et al., 2015;Zhang et al., 2022). Zhang et al. (2022) applied cryo-TEM to prove that the dry state of the phase-separated soot particles by TEM

analysis can represent the actual distribution of soot particles with LLPS under different RHs in ambient air. As we known, this study provides the first observation of the redistribution of soot particles in the air of eastern TP.

3.2 Relative abundance and size distribution of S-soot-OM-coating particle

Figure 4 displays the relative abundances of soot, S-soot, and S-soot-OM-coating particles in all soot-containing particles. The number contributions of S-soot-OM-coating particles to the total soot-containing particles ranged from 5.9% to 78.2% with an average value of 34.8% (Fig. 4a). A TEM image shows a significant number of S-soot-OM-coating particles in the sample collected at 10:00 on 23 June (Fig. 4b). The results indicate that a substantial amount of soot-containing particles may undergo the LLPS process during the sampling period.

Figure 5a shows that soot-containing particles predominantly occurred in the fine mode (<1 μm). The size distribution of soot and S-soot particles displayed the peak at 134 nm and 188 nm, respectively, indicating that a secondary sulfate coating enlarged soot-containing particle sizes (Fig. 5a). Figure 5b demonstrates that the relative abundance of S-soot-OM-coating particles increased as particle size increased, reaching nearly 70-80% for particles larger than 500 nm. The result is similar to the previous reports that particle size plays a crucial role to influence the LLPS of individual particles (Altaf et al., 2016;Li et al., 2021). Here we systematically investigate whether particle size can affect the redistribution of soot particles in S-soot-OM-coating particles.

3.3 Redistribution of soot particles in OM-coatings

Figure 6a shows that 73% of the S-soot-OM-coating particles were soot in OM-coating particles (named soot-Ocoating particles for short). 24% of the S-soot-OM-coating particles were fractional soot in the inorganic sulfate core and other soot in OM-coating (named soot-Icore-Ocoating particles for short) (Fig. 6a). The remaining 3% of the S-soot-OM-coating particles were all soot in the inorganic sulfate core (named soot-Icore particles for short) (Fig. 6a). The prevalence of soot-Ocoating particle at 73% in this study was notably higher than the reported 59% in the background air in northern and central China (Zhang et al., 2022). Therefore, we conclude that soot redistribution in secondary particles is a common occurrence on Mt. Emei during the sampling period. Zhang et al. (2022) suggested that the soot redistribution is primarily influenced by the OM-coating thickness and particle size. Similar to the method employed by Zhang et al. (2022), we calculated the OM-coating thicknesses and the entire particle sizes based on TEM and AFM (Figs. 7, S2, S3). Figure 6b shows that there is a certain positive correlation between the OM-coating thicknesses and the entire particle sizes, implying that larger S-soot-OM-coating particles tend to contain thicker OM-coating. The result well explains why the soot-Ocoating particles mostly had larger sizes (avg. 790 nm) and thicker coatings (avg. 50 nm) compared to soot-Icore-Ocoating particles (avg. 737 nm for particle size and 35 nm for coating thickness) and soot-Icore particles (avg. 571 nm for particle size and 19 nm for coating thickness) (Fig. 6b-e).

In this study, we employed the ratio of OM-coating thickness to soot size (OM/soot) as a tool to investigate the redistribution mechanisms of soot particles in S-soot-OM-coating particles. As illustrated in Figure 8a, the ratios of OM/soot in soot-

Ocoating particles were significantly higher (avg. 0.32) than those in both soot-Icore-Ocoating particles (avg. 0.24) and soot-Icore particles (avg. 0.12). To further explore this trend accurately, we divided the ratios into 15 bins between 0.1 and 0.4, which collectively accounted for over 80% of the total OM/soot ratios (Fig. 8b). We observed that when the OM/soot ratio was less than 0.1, all of S-soot-OM-coating particles were soot-Icore particles (Fig. 8b). As the ratio increased beyond 0.2, none of soot-Icore particles was observed, and nearly 60% of the total S-soot-OM-coating particles were identified as soot-Ocoating particles (Fig. 8b). When the ratio exceeded 0.32, more than 80% of the S-soot-OM-coating particles were identified as soot-Ocoating particles. Nearly all soot particles occurred in the OM-coating when the ratio of OM/soot was larger than 0.6 (Fig. 8b). These results suggest that soot exhibits a high likelihood of distributing into the organic coating instead of the inorganic core following an increasing ratio of OM/soot (Fig. 8b).

Zhang et al. (2022) reported that the dominant type of the laboratory-generated soot-containing particles shifts from soot-Icore particles to soot-Ocoating particles when the OM/soot ratio increased from 0.04 to 0.34. Their field-observed soot-containing particles were almost soot-Ocoating particles when the OM/soot ratio exceeded 0.24. Our study at 0.32 of the OM/soot was close to their laboratory results, suggesting the reliability of our research outcomes. However, our field observation was slightly higher than the previous reported 0.24, and this discrepancy could be attributed to the considerable presence of soot-Icore-Ocoating particles in our study, which was rarely observed in Zhang et al. (2022). Over 50% of soot particles were distributed within OM-coating in all the soot-Icore-Ocoating particles (as shown in the oblique bar in Fig. 8b). Consequently, combining the soot-Ocoating (brown bar in Fig. 8b) and soot in OM-coating of soot-Icore-Ocoating particles (oblique bar in Fig. 8b), we can infer that when the OM/soot ratio exceeds 0.2, most of soot (>80%) tend to distribute in organic phase in the atmosphere of Mt. Emei during sampling period (as indicated by the organics-dominated region in Fig. 8b). The TEM images clearly demonstrate the transferred position of soot from the inner sulfate core to the outer organic coatings following the increasing OM/soot (Fig. 8c-e).

In this study, we observed the distribution of multiple soot particles within the OM-coating (Fig. 8d), with approximately 27% of the total analysed S-soot-OM-coated particles containing one soot particle and 73% containing two or more soot particles in the OM-coating during the sampling period (Fig. 9a). We also found a positive correlation between the number of soot particles in the OM-coating and particle sizes (Fig. 9b). These results suggested that there was a higher tendency for multiple soot particles to distribute in the larger LLPS particles (Fig. 9c-e).

All of these observations provided evidence supporting the potential phenomenon of soot redistribution within LLPS particles in the atmosphere over the eastern TP. The soot redistribution is probably governed by the entire particle size and the ratio of OM-coating thickness to soot size.

3.4 D_f changes of soot particles after redistribution

To examine the specific morphological changes of soot particles, we calculated the D_f of externally mixed soot, sulfate-coated soot and organic-coated soot. Figure 10 and Table 1 show that the D_f sequence from low to high values is ranked as externally mixed soot (1.79±0.09) < sulfate-coated soot (1.84±0.07) < organic-coated soot (1.95±0.06). Higher D_f values

reflected a more compacted structure of the highly aged soot particles by internally mixing with sulfate and organics (Yuan et al., 2019;Wang et al., 2017b;China et al., 2015). In addition to D_f, the variation in morphological parameters such as *CV*, *RN* and *AR* can also indicate the morphological changes of individual soot particles on Mt. Emei (Table 1). The sulfate-coated soot and organic-coated soot particles had a higher *CV* (0.87 and 0.87, respectively), higher *RN* (0.41 and 0.42, respectively) and lower *AR* (1.61 and 1.61, respectively) than those of externally mixed soot (avg. *CV*=0.81, avg. *RN*=0.38, and avg. *AR*=1.63). The conclusion derived from all these morphological parameters was consistent with the compacted soot particles enclosed by sulfate and organics. Indeed, several field and laboratory studies found that soot embedded with sulfate and organics could increase its compactness after coating (Wang et al., 2021b;Xue et al., 2009;Saathoff et al., 2003).

4 Implications and summary

BC, as the most important light-absorbing aerosol, is a nonnegligible contributor to atmospheric warming over the Third Pole (Chen et al., 2022b;Zhang et al., 2021a;Cong et al., 2015;Zhang et al., 2021b). Given the high concentration of BC on the eastern TP (Yuan et al., 2020b), understanding the climate-related factors of BC in the eastern TP air, particularly the mixing state and ageing processes of soot particles, is imperative. In this study, ground-based sampling, electron microscopy analyses and theoretical calculations were used to investigate the atmospheric processes of soot particles on the eastern rim of the TP.

We analysed thousands of individual particles, and 54% of the total particles were soot-containing particles (Figs. S4 and 11). Electron microscopy analysis indicates that one-third of the total soot-containing particles exhibited a sulfate core–organic shell structure with soot distributed in either the inorganic core or the organic coating (S-soot-OM-coating particles). Long-range transported air masses from the highly polluted Sichuan Basin or interior TP could carry large amounts of anthropogenic pollutants to eastern TP air. The ageing process during long-range transport would result in an increase in the organic-coating thickness and entire particle sizes of S-soot-OM-coating particles.

Approximately 73% of the core–shell soot-containing particles may experience a redistribution process that drove soot from the inorganic phase to the organic phase. Our morphological analysis suggests that the entire particle size and ratio of organic coating thickness divided by the size of soot (OM/soot) are two of the major possible factors affecting the redistribution of soot. Once the OM/soot ratio exceeded 0.2, more than 80% of the soot tended to distribute in the organic coating (Figs. 8b, 11). Conversely, when the OM/soot ratio was less than 0.1, all of the soot in the S-soot-OM-coating particles was found in the sulfate core (Figs. 8b, 11). Consequently, larger particles with thicker organic coatings are more inclined to drive and capture more smaller soot particles from the inorganic phase to the organic phase.

Theoretical calculations have shown that aged soot particles that were internally mixed with sulfate and organics had higher D_f values (1.84±0.07 for sulfate-coated soot, 1.95±0.06 for organic-coated soot) than those of externally mixed soot (1.79±0.09). The assessment of the optical properties and climatic effects of soot particles is highly dependent on the shape

and position of the soot within the entire host particle (Adachi et al., 2010;Wang et al., 2021c;Zhang et al., 2022). It is important to quantify the key morphological parameters to serve the climatic simulation of BC in eastern TP air.

In summary, the outcomes of this investigation will enhance comprehension regarding the mixing structure and ageing process of BC in the TP atmosphere (Fig. 11). The discovery of BC redistribution following LLPS might be a widespread phenomenon across the entire TP. These findings will promote the future evaluation of the climatic effects of BC at the Third Pole.

Data availability. Data presented in this paper are available from https://doi.org/10.6084/m9.figshare.21988439.

Supplement. The supplement related to this article is available online.

Author contributions. WL and QY designed the research. QY performed the data analysis and wrote the manuscript, and WL revised it. SY assisted with the sample collection. YW, YC, JZ, YZ and LX carried out the TEM analysis of individual particles. WH, DL, PF, and HG contributed to the improvement of this paper. All the authors approved the final version of this paper.

Competing interest. At least one of the (co-)authors is a member of the editorial board of *Atmos. Chem. Phys.*. The peer-review process was guided by an independent editor, and the authors also have no other competing interests to declare.

Disclaimer. Publisher's note: Copernicus Publications remains neutral with regard to jurisdictional claims in published maps and institutional affiliations.

Financial support. This work was funded by Zhejiang Provincial Natural Science Foundation of China (LY21D050002), National Natural Science Foundation of China (91844301, 42075096), Fundamental Research Funds for the Central Universities (No. K20220232), LAC/CMA (2022B09).

References

Adachi, K., Chung, S. H., and Buseck, P. R.: Shapes of soot aerosol particles and implications for their effects on climate, J Geophys. Res.- Atmos., 115, 9, 10.1029/2009jd012868, 2010.

Adachi, K., and Buseck, P. R.: Changes of ns-soot mixing states and shapes in an urban area during CalNex, J Geophys. Res.- Atmos., 118, 3723-3730, 10.1002/jgrd.50321, 2013.

Adachi, K., Tobo, Y., Koike, M., Freitas, G., Zieger, P., and Krejci, R.: Composition and mixing state of Arctic aerosol and cloud residual particles from long-term single-particle observations at Zeppelin Observatory, Svalbard, Atmos. Chem. Phys., 22, 14421-14439, 10.5194/acp-22-14421-2022, 2022.

Altaf, M. B., Zuend, A., and Freedman, M. A.: Role of nucleation mechanism on the size dependent morphology of organic aerosol, Chem. Comm. , 52, 9220-9223, 10.1039/c6cc03826c, 2016.

Bond, T. C., Doherty, S. J., Fahey, D. W., Forster, P. M., Berntsen, T., DeAngelo, B. J., Flanner, M. G., Ghan, S., Karcher, B., Koch, D., Kinne, S., Kondo, Y., Quinn, P. K., Sarofim, M. C., Schultz, M. G., Schulz, M., Venkataraman, C., Zhang, H., Zhang, S., Bellouin, N., Guttikunda, S. K., Hopke, P. K., Jacobson, M. Z., Kaiser, J. W., Klimont, Z., Lohmann, U., Schwarz, J. P., Shindell, D., Storelvmo, T., Warren, S. G., and Zender, C. S.: Bounding the role of black carbon in the climate system: A scientific assessment, J Geophys. Res.-Atmos., 118, 5380-5552, 10.1002/jgrd.50171, 2013.

Brunamonti, S., Krieger, U. K., Marcolli, C., and Peter, T.: Redistribution of black carbon in aerosol particles undergoing liquid-liquid phase separation, Geophys. Res. Lett., 42, 2532-2539, 10.1002/2014GL062908, 2015.

Buseck, P. R., Adachi, K., Andras, G., Tompa, E., and Mihaly, P.: Ns-Soot: A Material-Based Term for Strongly Light-Absorbing Carbonaceous Particles, Aerosol Sci. Technol., 48, 777-788, 10.1080/02786826.2014.919374, 2014.

Chen, C., Fan, X. L., Shaltout, T., Qiu, C., Ma, Y., Goldman, A., and Khalizov, A. F.: An unexpected restructuring of combustion soot aggregates by subnanometer coatings of polycyclic aromatic hydrocarbons, Geophys. Res. Lett., 43, 11080-11088, 10.1002/2016gl070877, 2016.

Chen, L. Y., Zhang, J. K., Huang, X. J., Li, H., Dong, G. M., and Wei, S. Y.: Characteristics and pollution formation mechanism of atmospheric fine particles in the megacity of Chengdu, China, Atmos. Res., 273, 10.1016/j.atmosres.2022.106172, 2022a.

Chen, S. Y., Zhang, R. H., Mao, R., Zhang, Y. L., Chen, Y., Ji, Z. M., Gong, Y. Q., and Guan, Y. W.: Sources, characteristics and climate impact of light-absorbing aerosols over the Tibetan Plateau, Earth Sci. Rev., 232, 10.1016/j.earscirev.2022.104111, 2022b.

Chi, J. W., Li, W. J., Zhang, D. Z., Zhang, J. C., Lin, Y. T., Shen, X. J., Sun, J. Y., Chen, J. M., Zhang, X. Y., Zhang, Y. M., and Wang, W. X.: Sea salt aerosols as a reactive surface for inorganic and organic acidic gases in the Arctic troposphere, Atmos. Chem. Phys., 15, 11341-11353, 10.5194/acp-15-11341-2015, 2015.

China, S., Mazzoleni, C., Gorkowski, K., Aiken, A. C., and Dubey, M. K.: Morphology and mixing state of individual freshly emitted wildfire carbonaceous particles, Nat. Commun., 4, 2122, 10.1038/ncomms3122, 2013.

China, S., Scarnato, B., Owen, R. C., Zhang, B., Ampadu, M. T., Kumar, S., Dzepina, K., Dziobak, M. P., Fialho, P., Perlinger, J. A., Hueber, J., Helmig, D., Mazzoleni, L. R., and Mazzoleni, C.: Morphology and mixing state of aged soot particles at a remote marine free troposphere site: Implications for optical properties, Geophys. Res. Lett., 42, 1243-1250, 10.1002/2014gl062404, 2015.

Cong, Z. Y., Kang, S. C., Kawamura, K., Liu, B., Wan, X., Wang, Z., Gao, S., and Fu, P.: Carbonaceous aerosols on the south edge of the Tibetan Plateau: concentrations, seasonality and sources, Atmos. Chem. Phys., 15, 1573-1584, 10.5194/acp-15-1573-2015, 2015.

Dong, Z., Qin, D., Kang, S., Liu, Y., Li, Y., Huang, J., and Qin, X.: Individual particles of cryoconite deposited on the mountain glaciers of the Tibetan Plateau: Insights into chemical composition and sources, Atmos. Environ., 138, 114-124, 10.1016/j.atmosenv.2016.05.020, 2016.

Fierce, L., Onasch, T. B., Cappa, C. D., Mazzoleni, C., China, S., Bhandari, J., Davidovits, P., Fischer, D. A., Helgestad, T., Lambe, A. T., Sedlacek, A. J., Smith, G. D., and Wolff, L.: Radiative absorption enhancements by black carbon controlled by particle-to-particle heterogeneity in composition, Proc. Natl. Acad. Sci. USA, 117, 5196-5203, 10.1073/pnas.1919723117, 2020.

Freedman, M. A.: Phase separation in organic aerosol, Chem. Soc. Rev., 46, 7694-7705, 10.1039/C6CS00783J, 2017.

Freedman, M. A.: Liquid–Liquid Phase Separation in Supermicrometer and Submicrometer Aerosol Particles, Acc. Chem. Res., 53, 1102-1110, 10.1021/acs.accounts.0c00093, 2020.

Fu, Y., Peng, X., Sun, W., Hu, X., Wang, D., Yang, Y., Guo, Z., Wang, Y., Zhang, G., Zhu, J., Ou, J., Shi, Z., Wang, X., and Bi, X.: Impact of Cloud Process in the Mixing State and Microphysical Properties of Soot Particles: Implications in Light Absorption Enhancement, J Geophys. Res.- Atmos., 127, e2022JD037169, 10.1029/2022JD037169, 2022.

Han, H., Wu, Y., Liu, J., Zhao, T. L., Zhuang, B. L., Wang, H. L., Li, Y. C., Chen, H. M., Zhu, Y., Liu, H. N., Wang, Q. G., Li, S., Wang, T. J., Xie, M., and Li, M. M.: Impacts of atmospheric transport and biomass burning on the inter-annual variation in black carbon aerosols over the Tibetan Plateau, Atmos. Chem. Phys., 20, 13591-13610, 10.5194/acp-20-13591-2020, 2020.

He, C., Li, Q., Liou, K.-N., Takano, Y., Gu, Y., Qi, L., Mao, Y., and Leung, L. R.: Black carbon radiative forcing over the Tibetan Plateau, Geophys. Res. Lett., 41, 7806-7813, 10.1002/2014GL062191, 2014.

Hu, K., Liu, D., Tian, P., Wu, Y., Deng, Z., Wu, Y., Zhao, D., Li, R., Sheng, J., Huang, M., Ding, D., Li, W., Wang, Y., and Wu, Y.: Measurements of the Diversity of Shape and Mixing State for Ambient Black Carbon Particles, Geophys. Res. Lett., 48, e2021GL094522, 10.1029/2021GL094522, 2021.

Hu, T. F., Cao, J. J., Zhu, C. S., Zhao, Z. Z., Liu, S. X., and Zhang, D. Z.: Morphologies and elemental compositions of local biomass burning particles at urban and glacier sites in southeastern Tibetan Plateau: Results from an expedition in 2010, Sci. Total Environ., 628-629, 772-781, 10.1016/j.scitotenv.2018.02.073, 2018.

Immerzeel, W. W., van Beek, L. P. H., and Bierkens, M. F. P.: Climate change will affect the Asian Water Towers, Science, 328, 1382-1385, 10.1126/science.1183188, 2010.

Jia, R., Luo, M., Liu, Y. Z., Zhu, Q. Z., Hua, S., Wu, C. Q., and Shao, T. B.: Anthropogenic Aerosol Pollution over the Eastern Slope of the Tibetan Plateau, Adv. Atmos. Sci., 36, 847-862, 10.1007/s00376-019-8212-0, 2019.

Kang, S. C., Zhang, Y. L., Chen, P. F., Guo, J. M., Zhang, Q. G., Cong, Z. Y., Kaspari, S., Tripathee, L., Gao, T. G., Niu, H. W., Zhong, X. Y., Chen, X. T., Hu, Z. F., Li, X. F., Li, Y., Neupane, B., Yan, F. P., Rupakheti, D., Gul, C., Zhang, W., Wu, G. M., Yang, L., Wang, Z. Q.,

and Li, C. L.: Black carbon and organic carbon dataset over the Third Pole, Earth Syst.Sci. Data, 14, 683-707, 10.5194/essd-14-683-2022, 2022.

Kirpes, R. M., Lei, Z., Fraund, M., Gunsch, M. J., May, N. W., Barrett, T. E., Moffett, C. E., Schauer, A. J., Alexander, B., Upchurch, L. M., China, S., Quinn, P. K., Moffet, R. C., Laskin, A., Sheesley, R. J., Pratt, K. A., and Ault, A. P.: Solid organic-coated ammonium sulfate particles at high relative humidity in the summertime Arctic atmosphere, Proc. Natl. Acad. Sci. USA, 119, e2104496119, 10.1073/pnas.2104496119, 2022.

Kopacz, M., Mauzerall, D. L., Wang, J., Leibensperger, E. M., Henze, D. K., and Singh, K.: Origin and radiative forcing of black carbon transported to the Himalayas and Tibetan Plateau, Atmos. Chem. Phys., 11, 2837-2852, 10.5194/acp-11-2837-2011, 2011.

Koylu, U. O., Xing, Y. C., and Rosner, D. E.: Fractal morphology analysis of combustion-generated aggregates using angular light scattering and electron microscope images, Langmuir, 11, 4848-4854, 1995.

Leskinen, J., Hartikainen, A., Vaatainen, S., Ihalainen, M., Virkkula, A., Mesceriakovas, A., Tiitta, P., Miettinen, M., Lamberg, H., Czech, H., Yli-Pirila, P., Tissari, J., Jakobi, G., Zimmermann, R., and Sippula, O.: Photochemical Aging Induces Changes in the Effective Densities, Morphologies, and Optical Properties of Combustion Aerosol Particles, Environ. Sci. Technol., 57, 5137-5148, 10.1021/acs.est.2c04151, 2023.

Li, C. L., Bosch, C., Kang, S. C., Andersson, A., Chen, P. F., Zhang, Q. G., Cong, Z. Y., Chen, B., Qin, D. H., and Gustafsson, O.: Sources of black carbon to the Himalayan-Tibetan Plateau glaciers, Nat. Commun., 7, 7, 10.1038/ncomms12574, 2016a.

Li, W., Sun, J., Xu, L., Shi, Z., Riemer, N., Sun, Y., Fu, P., Zhang, J., Lin, Y., Wang, X., Shao, L., Chen, J., Zhang, X., Wang, Z., and Wang, W.: A conceptual framework for mixing structures in individual aerosol particles, J Geophys. Res.- Atmos., 121, 13784-13798, 10.1002/2016jd025252, 2016b.

Li, W., Liu, L., Xu, L., Zhang, J., Yuan, Q., Ding, X., Hu, W., Fu, P., and Zhang, D.: Overview of primary biological aerosol particles from a Chinese boreal forest: Insight into morphology, size, and mixing state at microscopic scale, Sci. Total Environ., 719, 137520, 10.1016/j.scitotenv.2020.137520, 2020.

Li, W., Liu, L., Zhang, J., Xu, L., Wang, Y., Sun, Y., and Shi, Z.: Microscopic Evidence for Phase Separation of Organic Species and Inorganic Salts in Fine Ambient Aerosol Particles, Environ. Sci. Technol., 55, 2234-2242, 10.1021/acs.est.0c02333, 2021.

Li, X., Kang, S., Zhang, G., Qu, B., Tripathee, L., Paudyal, R., Jing, Z., Zhang, Y., Yan, F., Li, G., Cui, X., Xu, R., Hu, Z., and Li, C.: Light-absorbing impurities in a southern Tibetan Plateau glacier: Variations and potential impact on snow albedo and radiative forcing, Atmos. Res., 200, 77-87, 10.1016/j.atmosres.2017.10.002, 2018.

Liu, H., Wang, Q., Xing, L., Zhang, Y., Zhang, T., Ran, W., and Cao, J.: Measurement report: quantifying source contribution of fossil fuels and biomass-burning black carbon aerosol in the southeastern margin of the Tibetan Plateau, Atmos. Chem. Phys., 21, 973-987, 10.5194/acp-21-973-2021, 2021.

Long, C. M., Nascarella, M. A., and Valberg, P. A.: Carbon black vs. black carbon and other airborne materials containing elemental carbon: Physical and chemical distinctions, Environ. Pollut., 181, 271-286, 10.1016/j.envpol.2013.06.009, 2013.

Pang, Y., Wang, Y., Wang, Z., Zhang, Y., Liu, L., Kong, S., Liu, F., Shi, Z., and Li, W.: Quantifying the Fractal Dimension and Morphology of Individual Atmospheric Soot Aggregates, J Geophys. Res.- Atmos., 127, e2021JD036055, 10.1029/2021JD036055, 2022.

Riemer, N., Ault, A. P., West, M., Craig, R. L., and Curtis, J. H.: Aerosol Mixing State: Measurements, Modeling, and Impacts, Rev. Geophys., 57, 187-249, 10.1029/2018rg000615, 2019.

Saathoff, H., Naumann, K. H., Schnaiter, M., Schock, W., Mohler, O., Schurath, U., Weingartner, E., Gysel, M., and Baltensperger, U.: Coating of soot and $(NH_4)_2SO_4$ particles by ozonolysis products of alpha-pinene, J. Aerosol. Sci., 34, 1297-1321, 10.1016/s0021-8502(03)00364-1, 2003.

Shao, L., Hu, Y., Fan, J., Wang, J., Wang, J., and Ma, J.: Physicochemical Characteristics of Aerosol Particles in the Tibetan Plateau: Insights from TEM-EDX Analysis, J. Nanosci. Nanotechnol., 17, 6899-6908, 10.1166/jnn.2017.14472, 2017.

Shi, Z. B., Zhang, D. Z., Ji, H. Z., Hasegawa, S., and Hayashi, M.: Modification of soot by volatile species in an urban atmosphere, Sci. Total Environ., 389, 195-201, 10.1016/j.scitotenv.2007.08.016, 2008.

Shu, Z., Liu, Y., Zhao, T., Zhou, Y., Habtemicheal, B. A., Shen, L., Hu, J., Ma, X., and Sun, X.: Long-term variations in aerosol optical properties, types, and radiative forcing in the Sichuan Basin, Southwest China, Sci. Total Environ., 807, 151490, 10.1016/j.scitotenv.2021.151490, 2022.

Tan, T., Hu, M., Du, Z., Zhao, G., Shang, D., Zheng, J., Qin, Y., Li, M., Wu, Y., Zeng, L., Guo, S., and Wu, Z.: Measurement report: Strong light absorption induced by aged biomass burning black carbon over the southeastern Tibetan Plateau in pre-monsoon season, Atmos. Chem. Phys., 21, 8499-8510, 10.5194/acp-21-8499-2021, 2021.

Wang, H.: Formation of nascent soot and other condensed-phase materials in flames, Proc. Combust. Inst., 33, 41-67, 10.1016/j.proci.2010.09.009, 2011.

Wang, J. F., Zhang, Q., Chen, M. D., Collier, S., Zhou, S., Ge, X. L., Xu, J. Z., Shi, J. S., Xie, C. H., Hu, J. L., Ge, S., Sun, Y. L., and Coe, H.: First chemical characterization of refractory black carbon aerosols and associated coatings over the Tibetan Plateau (4730 m a.s.l), Environ. Sci. Technol., 51, 14072-14082, 10.1021/acs.est.7b03973, 2017a.

Wang, Q. Y., Cao, J. J., Han, Y. M., Tian, J., Zhu, C. S., Zhang, Y. G., Zhang, N. N., Shen, Z. X., Ni, H. Y., Zhao, S. Y., and Wu, J. R.: Sources and physicochemical characteristics of black carbon aerosol from the southeastern Tibetan Plateau: internal mixing enhances light absorption, Atmos. Chem. Phys., 18, 4639-4656, 10.5194/acp-18-4639-2018, 2018.

Wang, T. T., Zhao, G., Tan, T. Y., Yu, Y., Tang, R. Z., Dong, H. B., Chen, S. Y., Li, X., Lu, K. D., Zeng, L. M., Gao, Y. Q., Wang, H. L., Lou, S. R., Liu, D. T., Hu, M., Zhao, C. S., and Guo, S.: Effects of biomass burning and photochemical oxidation on the black carbon mixing state and light absorption in summer season, Atmos. Environ., 248, 10.1016/j.atmosenv.2021.118230, 2021a.

Wang, Y., Li, W., Huang, J., Liu, L., Pang, Y., He, C., Liu, F., Liu, D., Bi, L., Zhang, X., and Shi, Z.: Nonlinear Enhancement of Radiative Absorption by Black Carbon in Response to Particle Mixing Structure, Geophys. Res. Lett., 48, e2021GL096437, 10.1029/2021GL096437, 2021b.

Wang, Y. Y., Liu, F. S., He, C. L., Bi, L., Cheng, T. H., Wang, Z. L., Zhang, H., Zhang, X. Y., Shi, Z. B., and Li, W. J.: Fractal dimensions and mixing structures of soot particles during atmospheric processing, Environ. Sci. Technol. Lett., 4, 487-493, 10.1021/acs.estlett.7b00418, 2017b.

Wang, Y. Y., Pang, Y. E., Huang, J., Bi, L., Che, H. Z., Zhang, X. Y., and Li, W. J.: Constructing Shapes and Mixing Structures of Black Carbon Particles With Applications to Optical Calculations, J Geophys. Res.- Atmos., 126, 10.1029/2021jd034620, 2021c.

Xu, B. Q., Cao, J. J., Hansen, J., Yao, T. D., Joswia, D. R., Wang, N. L., Wu, G. J., Wang, M., Zhao, H. B., Yang, W., Liu, X. Q., and He, J. Q.: Black soot and the survival of Tibetan glaciers, Proc. Natl. Acad. Sci. U. S. A., 106, 22114-22118, 10.1073/pnas.0910444106, 2009.

Xu, L., Fukushima, S., Sobanska, S., Murata, K., Naganuma, A., Liu, L., Wang, Y., Niu, H., Shi, Z., Kojima, T., Zhang, D., and Li, W.: Tracing the evolution of morphology and mixing state of soot particles along with the movement of an Asian dust storm, Atmos. Chem. Phys., 20, 14321-14332, 10.5194/acp-20-14321-2020, 2020.

Xue, H. X., Khalizov, A. F., Wang, L., Zheng, J., and Zhang, R. Y.: Effects of coating of dicarboxylic acids on the mass-mobility relationship of soot particles, Environ. Sci. Technol., 43, 2787-2792, 10.1021/es803287v, 2009.

Yao, T., Thompson, L. G., Mosbrugger, V., Zhang, F., Ma, Y., Luo, T., Xu, B., Yang, X., Joswiak, D. R., Wang, W., Joswiak, M. E., Devkota, L. P., Tayal, S., Jilani, R., and Fayziev, R.: Third Pole Environment (TPE), Environ. Dev., 3, 52-64, 10.1016/j.envdev.2012.04.002, 2012a.

Yao, T. D., Thompson, L., Yang, W., Yu, W. S., Gao, Y., Guo, X. J., Yang, X. X., Duan, K. Q., Zhao, H. B., Xu, B. Q., Pu, J. C., Lu, A. X., Xiang, Y., Kattel, D. B., and Joswiak, D.: Different glacier status with atmospheric circulations in Tibetan Plateau and surroundings, Nat. Clim. Chang., 2, 663-667, 10.1038/nclimate1580, 2012b.

You, Y., Renbaum-Wolff, L., Carreras-Sospedra, M., Hanna, S. J., Hiranuma, N., Kamal, S., Smith, M. L., Zhang, X., Weber, R. J., Shilling, J. E., Dabdub, D., Martin, S. T., and Bertram, A. K.: Images reveal that atmospheric particles can undergo liquid–liquid phase separations, Proc. Natl. Acad. Sci. USA, 109, 13188-13193, doi:10.1073/pnas.1206414109, 2012.

Yu, H., Li, W., Zhang, Y., Tunved, P., Dall'Osto, M., Shen, X., Sun, J., Zhang, X., Zhang, J., and Shi, Z.: Organic coating on sulfate and soot particles during late summer in the Svalbard Archipelago, Atmos. Chem. Phys., 19, 10433-10446, 10.5194/acp-19-10433-2019, 2019.

Yuan, Q., Xu, J., Wang, Y., Zhang, X., Pang, Y., Liu, L., Bi, L., Kang, S., and Li, W.: Mixing State and Fractal Dimension of Soot Particles at a Remote Site in the Southeastern Tibetan Plateau, Environ. Sci. Technol., 53, 8227-8234, 10.1021/acs.est.9b01917, 2019.

Yuan, Q., Wan, X., Cong, Z., Li, M., Liu, L., Shu, S., Liu, R., Xu, L., Zhang, J., Ding, X., and Li, W.: In Situ Observations of Light-Absorbing Carbonaceous Aerosols at Himalaya: Analysis of the South Asian Sources and Trans-Himalayan Valleys Transport Pathways, J Geophys. Res.- Atmos., 125, e2020JD032615, 10.1029/2020jd032615, 2020a.

Yuan, Q., Xu, J., Liu, L., Zhang, A., Liu, Y., Zhang, J., Wan, X., Li, M., Qin, K., Cong, Z., Wang, Y., Kang, S., Shi, Z., Pósfai, M., and Li, W.: Evidence for Large Amounts of Brown Carbonaceous Tarballs in the Himalayan Atmosphere, Environ. Sci. Technol. Lett., 8, 16-23, 10.1021/acs.estlett.0c00735, 2021.

Yuan, T., Chen, S., Wang, L., Yang, Y., Bi, H., Zhang, X., and Zhang, Y.: Impacts of Two East Asian Atmospheric Circulation Modes on Black Carbon Aerosol Over the Tibetan Plateau in Winter, J Geophys. Res.- Atmos., 125, e2020JD032458, 10.1029/2020JD032458, 2020b.

Zhai, J., Yang, X., Li, L., Bai, B., Liu, P., Huang, Y., Fu, T.M., Zhu, L., Zeng, Z., Tao, S., Lu, X., Ye, X., Wang, X., Wang, L., and Chen, J.: Absorption Enhancement of Black Carbon Aerosols Constrained by Mixing-State Heterogeneity, Environ. Sci. Technol., 56, 1586-1593, 10.1021/acs.est.1c06180, 2022.

Zhang, J., Wang, Y., Teng, X., Liu, L., Xu, Y., Ren, L., Shi, Z., Zhang, Y., Jiang, J., Liu, D., Hu, M., Shao, L., Chen, J., Martin, S. T., Zhang, X., and Li, W.: Liquid-liquid phase separation reduces radiative absorption by aged black carbon aerosols, Comm. Earth Environ., 3, 128, 10.1038/s43247-022-00462-1, 2022.

Zhang, L., Tang, C., Huang, J., Du, T., Guan, X., Tian, P., Shi, J., Cao, X., Huang, Z., Guo, Q., Zhang, H., Wang, M., Zeng, H., Wang, F., and Dolkar, P.: Unexpected High Absorption of Atmospheric Aerosols Over a Western Tibetan Plateau Site in Summer, J Geophys. Res.- Atmos., 126, e2020JD033286, 10.1029/2020JD033286, 2021a.

Zhang, R., Wang, H., Qian, Y., Rasch, P. J., Easter, R. C., Ma, P. L., Singh, B., Huang, J., and Fu, Q.: Quantifying sources, transport, deposition, and radiative forcing of black carbon over the Himalayas and Tibetan Plateau, Atmos. Chem. Phys., 15, 6205-6223, 10.5194/acp-15-6205-2015, 2015.

Zhang, X. H., Xu, J. Z., Kang, S. C., Sun, J. Y., Shi, J. S., Gong, C. S., Sun, X. Y., Du, H. L., Ge, X. L., and Zhang, Q.: Regional Differences in the Light Absorption Properties of Fine Particulate Matter Over the Tibetan Plateau: Insights From HR-ToF-AMS and Aethalometer Measurements, J Geophys. Res.- Atmos., 126, 10.1029/2021jd035562, 2021b.

Zhang, X. Y., Wang, Y. Q., Niu, T., Zhang, X. C., Gong, S. L., Zhang, Y. M., and Sun, J. Y.: Atmospheric aerosol compositions in China: spatial/temporal variability, chemical signature, regional haze distribution and comparisons with global aerosols, Atmos. Chem. Phys., 12, 779-799, 10.5194/acp-12-779-2012, 2012.

Zhao, Y., Ren, H., Deng, J. J., Li, L. J., Hu, W., Ren, L. J., Yue, S. Y., Fan, Y. B., Wu, L. B., Li, J., Sun, Y. L., Wang, Z. F., Akimoto, H., Zeng, X., Cheng, Y., Kong, S. F., Su, H., Cheng, Y. F., Kawamura, K., and Fu, P. Q.: High daytime abundance of primary organic aerosols over Mt. Emei, Southwest China in summer, Sci. Total Environ., 703, 13, 10.1016/j.scitotenv.2019.134475, 2020.

Zhao, Z. Z., Wang, Q. Y., Xu, B. Q., Shen, Z. X., Huang, R. J., Zhu, C. S., Su, X. L., Zhao, S. Y., Long, X., Liu, S. X., and Cao, J. J.: Black carbon aerosol and its radiative impact at a high-altitude remote site on the southeastern Tibet Plateau, J Geophys. Res.- Atmos., 122, 5515-5530, 10.1002/2016jd026032, 2017.

Zhu, C. S., Qu, Y., Huang, H., Chen, J., Dai, W. T., Huang, R. J., and Cao, J. J.: Black Carbon and Secondary Brown Carbon, the Dominant Light Absorption and Direct Radiative Forcing Contributors of the Atmospheric Aerosols Over the Tibetan Plateau, Geophys. Res. Lett., 48, 10.1029/2021gl092524, 2021.

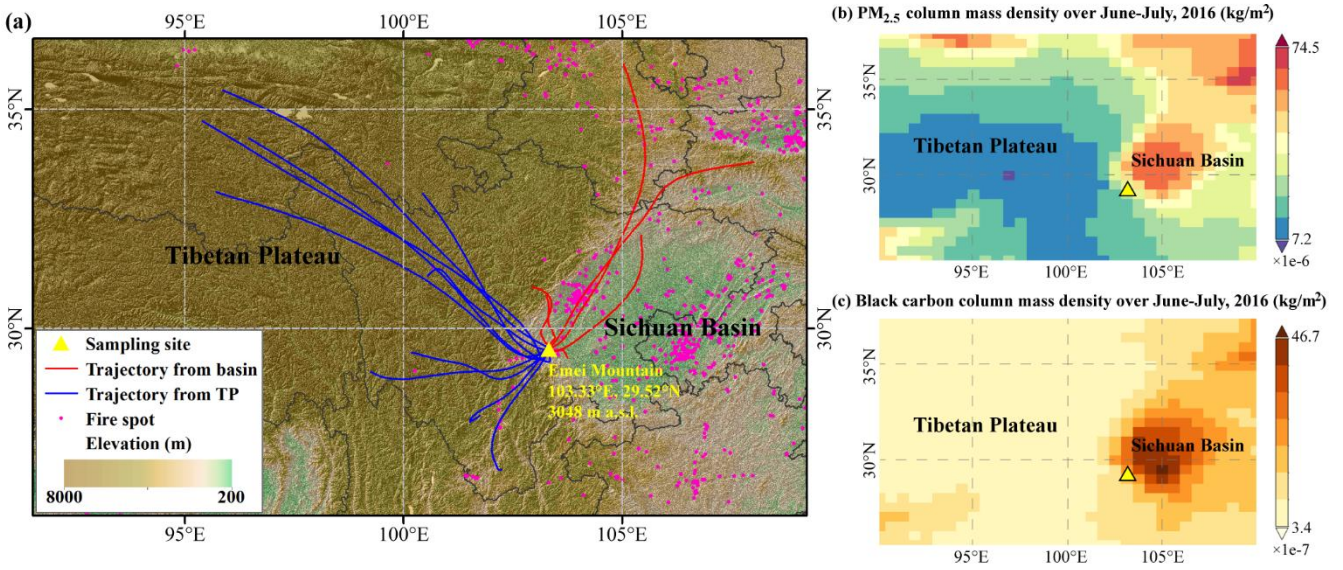

Figure 1. Location of the sampling site, twenty-four-hour backwards trajectories during 22 June–9 July 2016, and $PM_{2.5}$ and BC column mass density covering the eastern TP and Sichuan Basin in June–July 2016. (a) Location of the sampling site with the Sichuan Basin on the eastern side and the TP on the western side (103.33°E, 29.52°N, 3048 m a.s.l. – above sea level). The twenty-four-hour backwards trajectories of each individual particle sample collection time were calculated using the Hybrid Single Particle Lagrange Integrated Trajectory model (HYSPLIT). Blue lines represent the western TP trajectories, and red lines represent the eastern basin trajectories. (b-c) $PM_{2.5}$ and BC column mass density covering the eastern TP and Sichuan Basin in June–July 2016 (Giovanni online data system, https://giovanni.gsfc.nasa.gov/giovanni/).

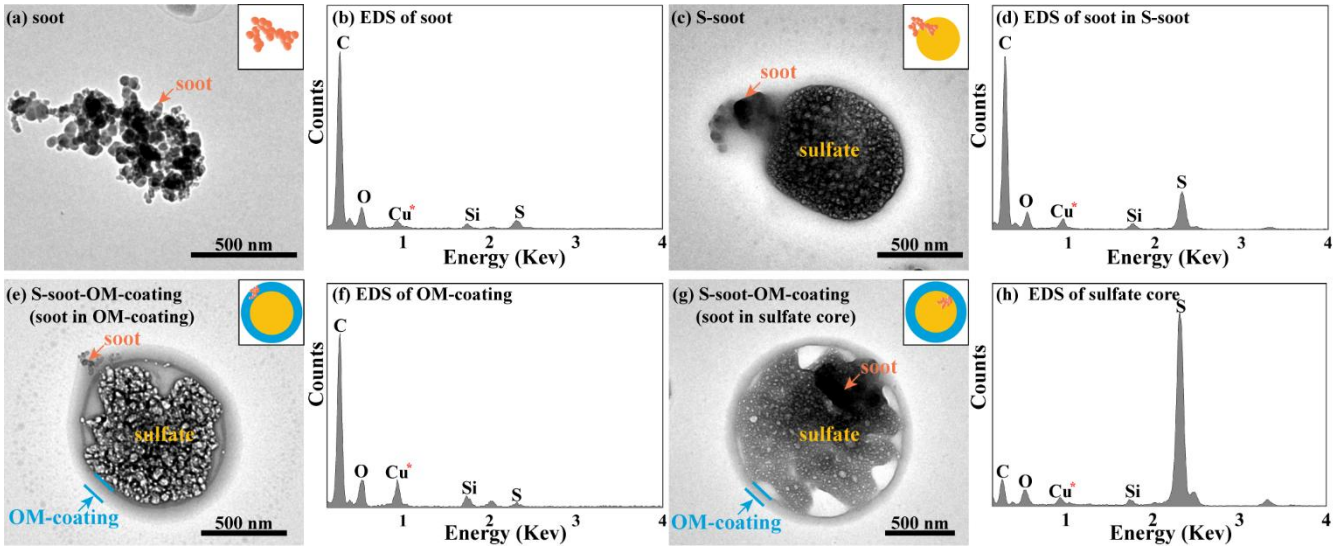

Figure 2. The major types of soot-containing particles in this study. (a) A TEM image of soot. (b) EDS spectrum of soot. Asterisk represents Cu, which was excluded from the EDS detection due to the copper material of TEM grids. (c) A TEM image of S-soot. (d) EDS spectrum of soot in S-soot. (e) A TEM image of the S-soot-OM-coating with soot in the OM-coating. (f) EDS spectrum of OM-coating. (g) A TEM image of the S-soot-OM-coating with soot in the sulfate core. (h) EDS spectrum of the sulfate core. All conceptual graphs are placed in the top right corner of each image. The orange-circle aggregates, yellow circles, and blue rings represent soot, sulfate, and OM-coatings, respectively.

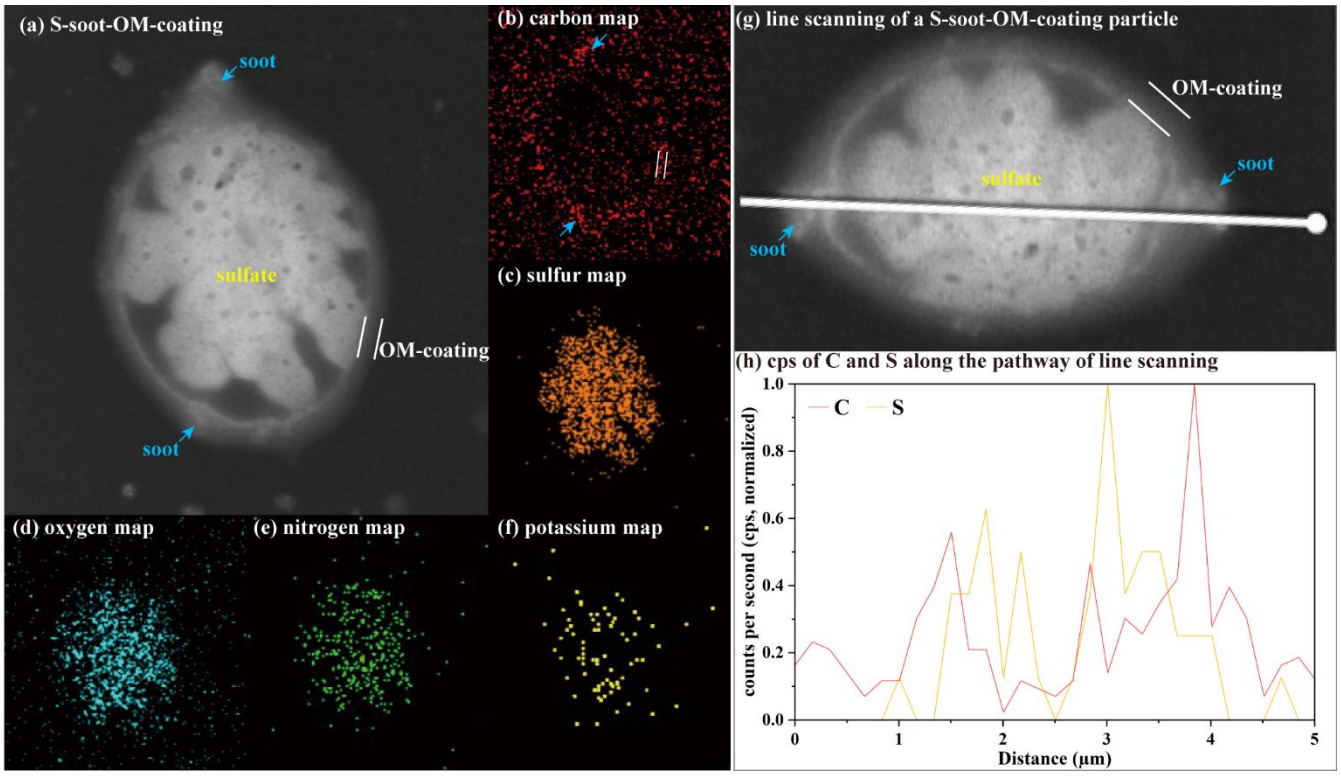

Figure 3. Elemental distribution in individual S-soot-OM-coating particles. (a) A dark-field TEM image of a S-soot-OM-coating particle. (b-f) TEM-EDS elemental maps of C, S, O, N, and K of the S-soot-OM-coating particle. (g) A TEM image of a S-soot-OM-coating particle for line scanning detection. (h) Counts per second (cps) of C and S along the pathway of line scanning over the S-soot-OM-coating particle.

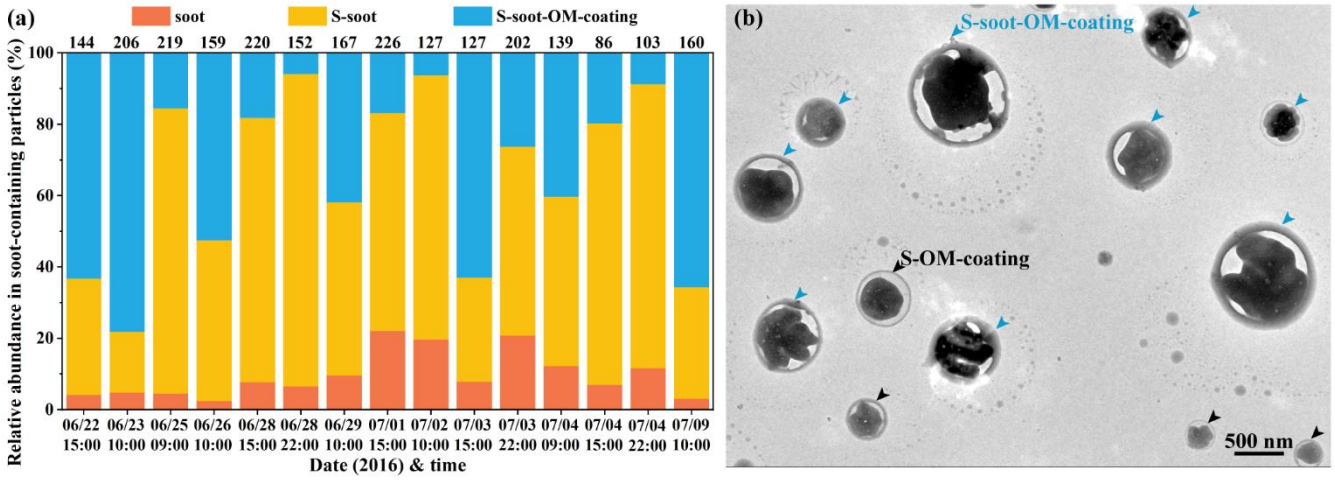

Figure 4. (a) Relative abundance of soot, S-soot and S-soot-OM-coating particles in all soot-containing particles at the Mt. Emei site at each sampling time from 22 June to 09 July 2016. A total of 2437 soot-containing particles were analysed, and the number of analysed particles is shown above the column. (b) A typical TEM image with abundant S-soot-OM-coating particles in the sample at 10:00 on 23 June.

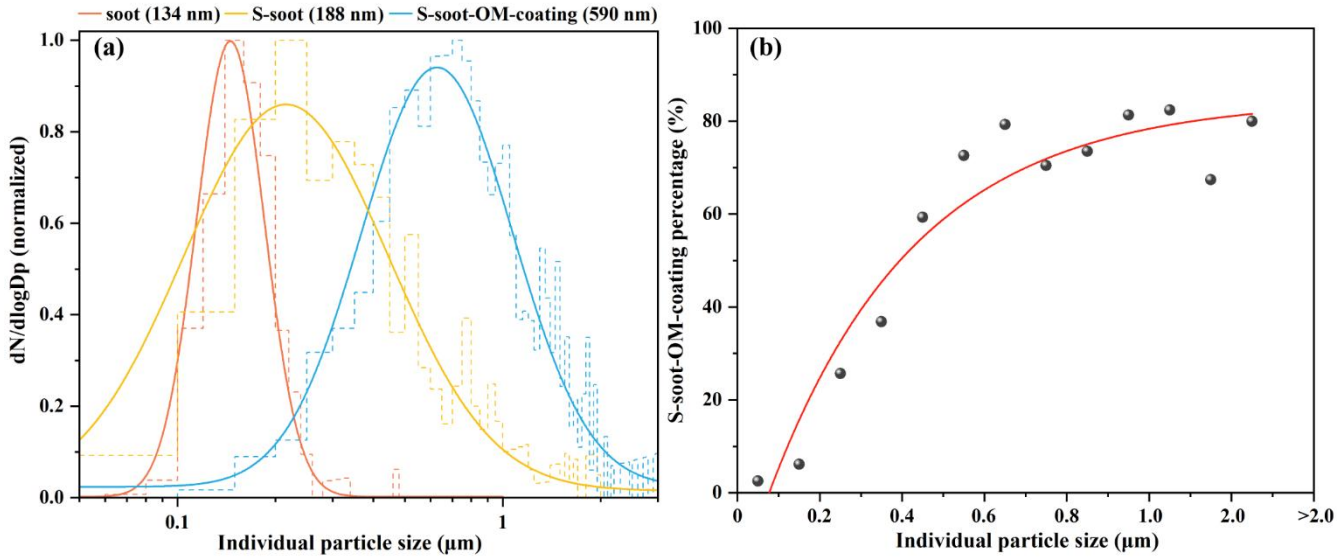

Figure 5. (a) Size distributions of soot, S-soot and S-soot-OM-coating particles. The numbers in parentheses represent the log-normal peaks. (b) Variations in the percentage of S-soot-OM-coating particles in all soot-containing particles with sizes.

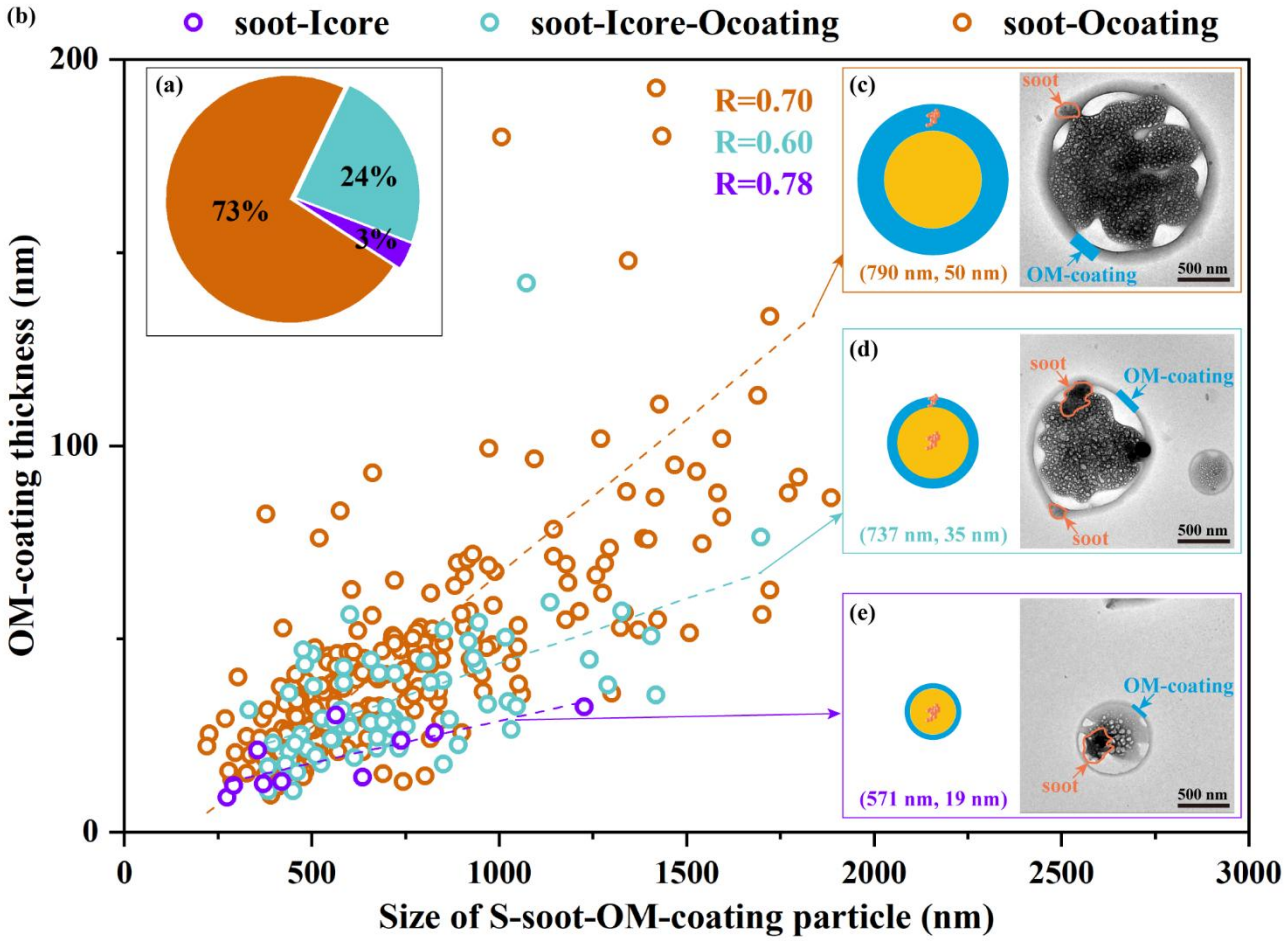

530

Figure 6. (a) The proportions of soot-Icore, soot-Icore-Ocoating, and soot-Ocoating particles in all S-soot-OM-coating particles. (b) The scatter distribution of entire particle sizes and OM-coating thicknesses of the analysed S-soot-OM-coating particles. Conceptual graphs and TEM images of (c) a soot-Ocoating particle, (d) a soot-Icore-Ocoating particle, and (e) a soot-Icore particle. The first and second number in each parenthesis represents the average size and OM-coating thickness of the corresponding S-
535 **soot-OM-coating particle, respectively.**

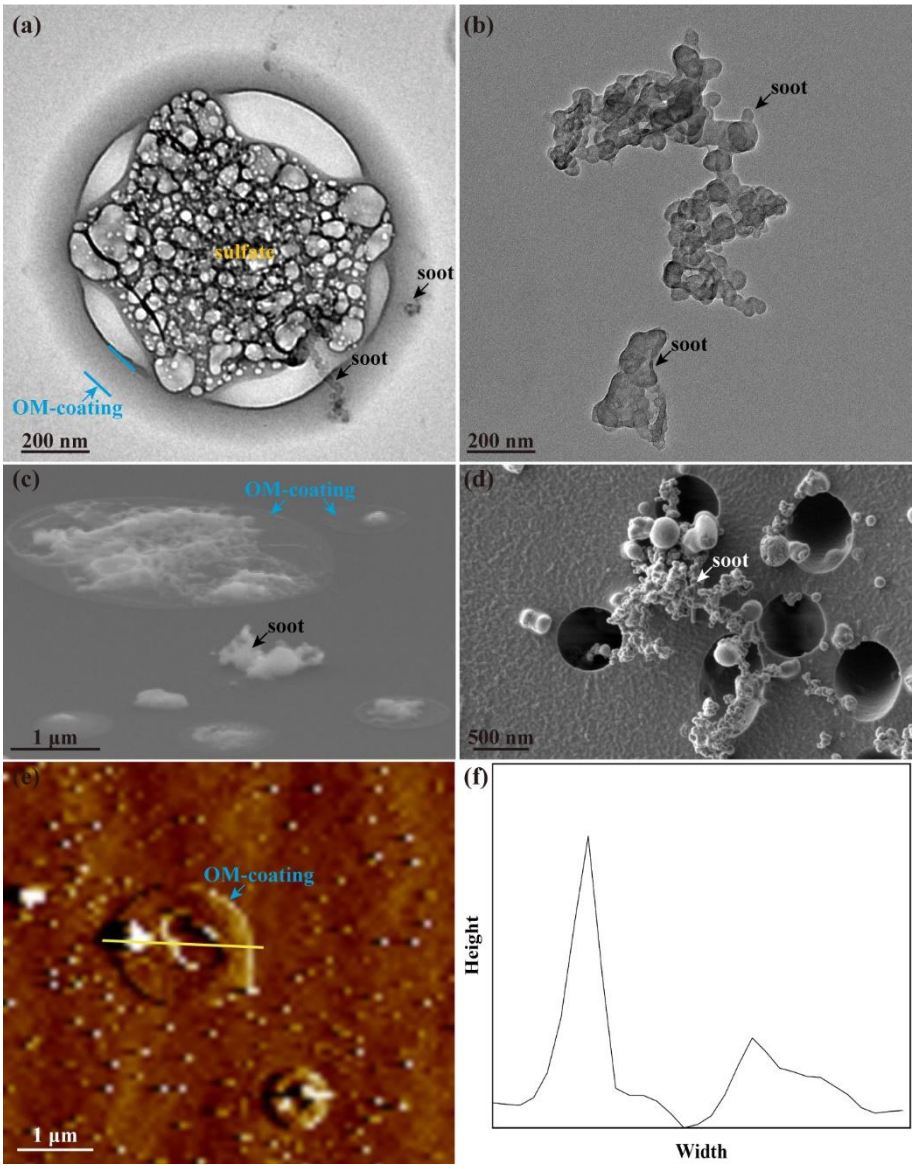

Figure 7. Different views from the different microscopic techniques. (a) A TEM image of S-soot-OM-coating particle, (b) A TEM image of soot particles, (c) A SEM image at 75° tilt angle of individual particles, (d) A SEM image of soot particles, (e) An AFM image of S-soot-OM-coating particle, (f) The cross-sectional analysis from the left AFM image.

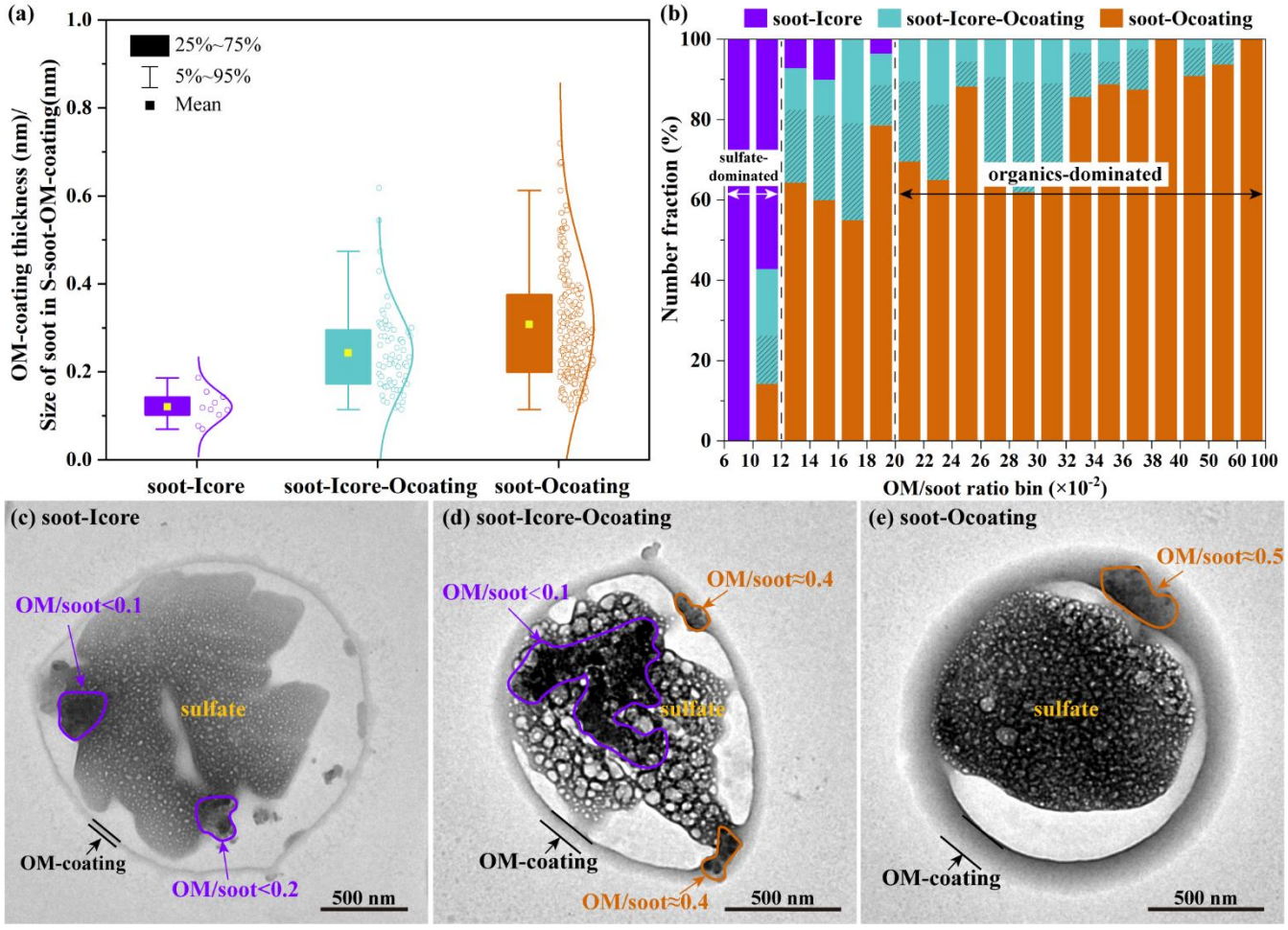

Figure 8. Variations of OM/soot ratios with different distribution positions of soot in S-soot-OM-coating particles. (a) The different ratios of OM/soot in the S-soot-OM-coating particles. (b) Number fractions of soot-Icore, soot-Icore-Ocoating, and soot-Ocoating particles in all S-soot-OM-coating particles in different ratios of OM/soot. Oblique bar represents that soot were distributed within OM-coating in all of the soot-Icore-Ocoating particles. (c) A typical TEM image of a soot-Icore particle with two soot particles in a sulfate core (OM/soot<0.2). (d) A typical TEM image of a soot-Icore-Ocoating particle with a soot particle in a sulfate core (OM/soot<0.1) and two soot particles in an OM-coating (OM/soot≈0.4). (e) A typical TEM image of a soot-Ocoating particle with a soot particle in the OM-coating (OM/soot≈0.5).

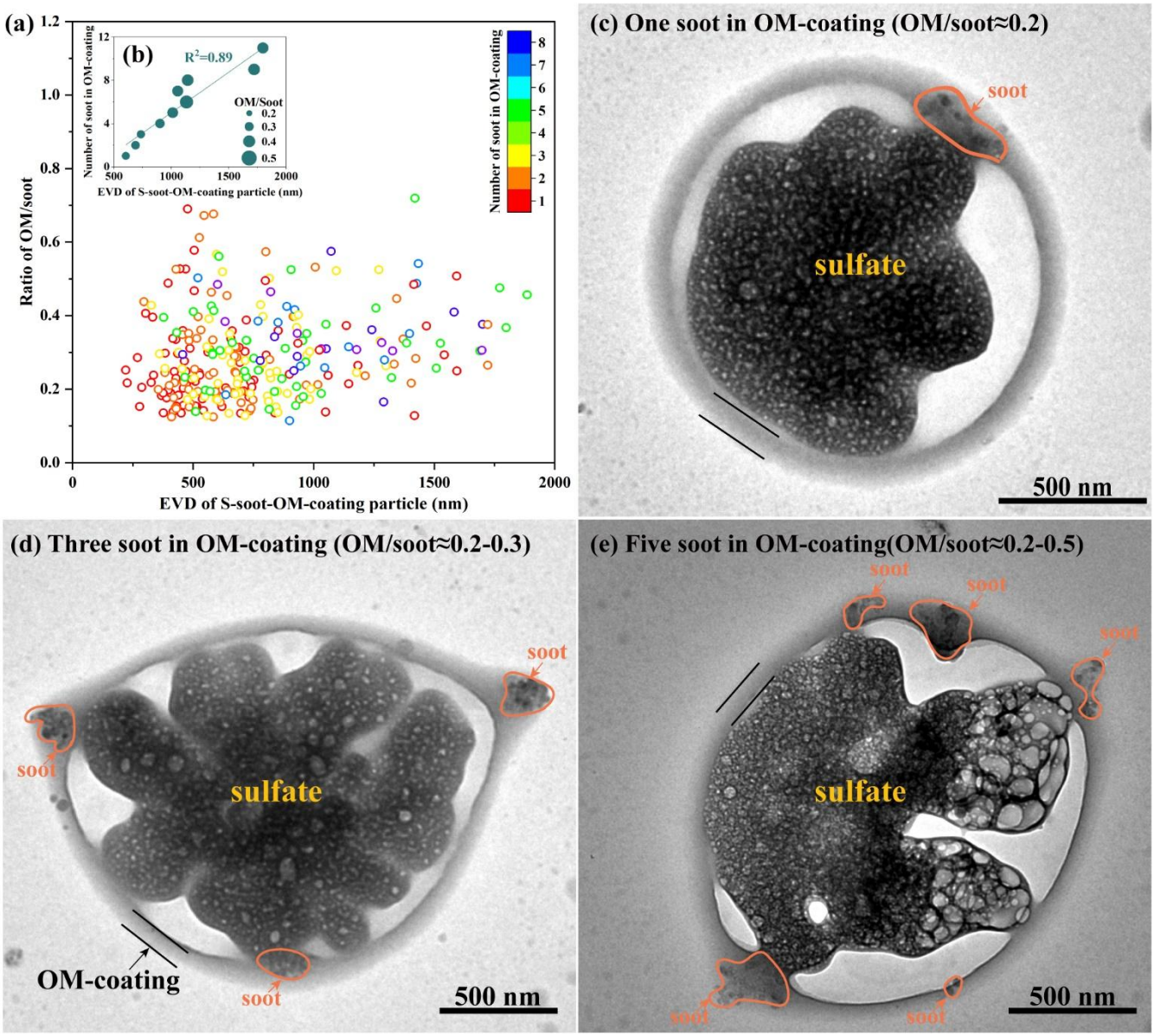

Figure 9. (a) Scatter diagram of OM/soot and the entire particle size of the S-soot-OM-coating particles. Different colours represent the number of soot particles being captured in the OM-coating. (b) Correlation between the average size of the S-soot-OM-coating particle and the average number of soot particles in the OM-coating. The size of the circle point represents the average ratio of OM/soot. (c) A typical TEM image of a S-soot-OM-coating particle with one soot particle in an OM-coating (OM/soot≈0.2, the size of S-soot-OM-coating≈336 nm). (d) A typical TEM image of a S-soot-OM-coating particle with three soot particles in an OM-coating (OM/soot≈0.2-0.3, the size of S-soot-OM-coating≈652 nm). (e) A typical TEM image of a S-soot-OM-coating particle with five soot particles in an OM-coating (OM/soot≈0.2-0.5, the size of S-soot-OM-coating≈582 nm).

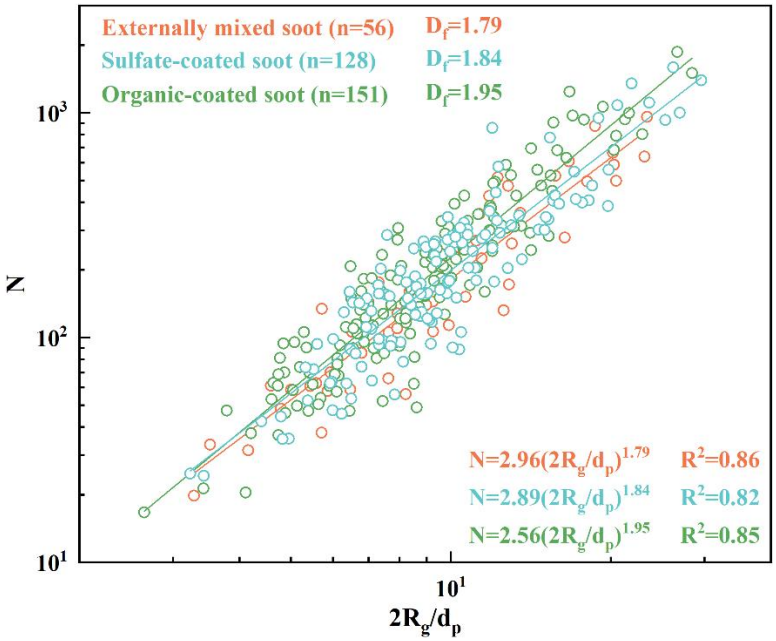

Figure 10. Fractal Dimension (D_f) of externally mixed soot, sulfate-coated soot and organic-coated soot on Mt. Emei. The parameter n in parenthesis represents the total number of soot particles analysed for each soot category to calculate D_f.

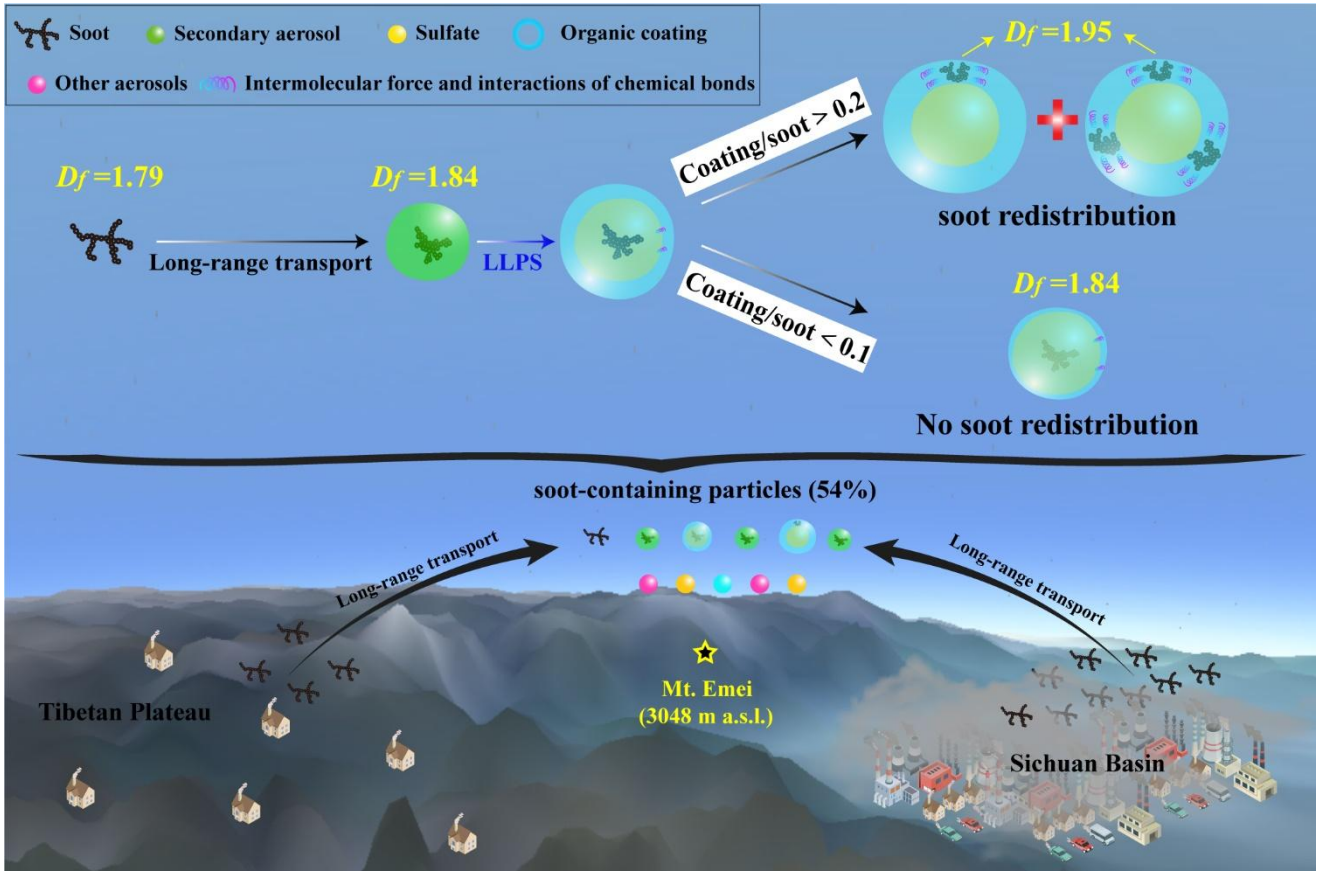

Figure 11. A conceptual model illustrating the atmospheric processes of soot on the eastern rim of the Tibetan Plateau.

Table 1. Morphological descriptors of soot particles on Mt. Emei during noncloud periods

Parameters[a]	soot	Sulfate-coated soot	Organic-coated soot
D_f	1.79 (0.09)	1.84 (0.07)	1.95 (0.06)
CV	0.81 (0.10)	0.87 (0.09)	0.87 (0.08)
RN	0.38 (0.20)	0.41 (0.20)	0.42 (0.21)
AR	1.63 (0.41)	1.61 (0.39)	1.61 (0.42)

[a]D_f, mass fractal dimension; *CV*, convexity of soot particles; *RN*, roundness of soot particles; *AR*, aspect ratio of soot particles. In parenthesis: standard error (*s.e.*). The standard error for D_f was calculated from the uncertainty in the mean-square fit considering the uncertainty in N and d_p.